Effects of cloud overlap in photochemical models

Yan Feng, Joyce E. Penner, Sanford Sillman, and Xiaohong Liu
Department of Atmospheric, Oceanic, and Space Sciences, University of Michigan, Ann Arbor, Michigan, USA

Received 3 August 2003; revised 17 December 2003; accepted 6 January 2004; published 25 February 2004.

[1] Different schemes have been used to represent the vertical coherence of clouds for radiation and cloud microphysics in general circulation models and for photolysis in photochemical transport models. Here, we examine the maximum-random overlap scheme, the random overlap scheme, and a linear scheme (linear scaling of the cloud optical depth in a grid box with cloud fraction) and evaluate their effects on averaged photolysis frequencies and OH concentrations in a global photochemical model. Photolysis frequencies are increased in the upper tropical troposphere and decreased in the lower troposphere if clouds are assumed to be randomly overlapped or if a linear assumption is followed rather than the maximum-random overlap assumption. The underestimate is of order 50% and 20–30% at the surface in the tropics and over some continental midlatitude regions for the linear and the random assumptions, respectively, relative to the maximum-random assumption. The global average CH_4 + OH reaction rate-weighted OH concentration calculated with the random overlap assumption is within a few percent of that calculated with the maximum-random overlap assumption but is underestimated with the nonphysically based linear assumption, by 4 to 6% relative to the maximum-random overlap assumption and by 6 to 7% relative to the random overlap assumption. An underestimate of rate-weighted OH concentration implies that the tropospheric lifetime for CH_4 and other greenhouse gases that react with OH is too long in models that use this scheme. *INDEX TERMS:* 0345 Atmospheric Composition and Structure: Pollution—urban and regional (0305); 0365 Atmospheric Composition and Structure: Troposphere—composition and chemistry; 0368 Atmospheric Composition and Structure: Troposphere—constituent transport and chemistry

Citation: Feng, Y., J. E. Penner, S. Sillman, and X. Liu (2004), Effects of cloud overlap in photochemical models, *J. Geophys. Res.*, *109*, D04310, doi:10.1029/2003JD004040.

1. Introduction

[2] Clouds within global models are usually represented by parameterizations that provide the liquid water path and cloud fraction associated with large scale (or stratiform) clouds and with convective clouds. This introduces the issue of how to represent the vertical coherence of clouds for radiative transfer and photochemical calculations. The most common cloud overlap assumptions used in the radiation and cloud microphysics schemes of general circulation models (GCMs) are the random and the maximum-random overlap assumptions (hereafter referred to as RAN and MRAN) [e.g., *Rotstayn*, 1997; *Wang and Rossow*, 1998; *Jakob and Klein*, 1999; *Morcrette and Jakob*, 2000; *Collins*, 2001]. Maximum-random overlap assumes that clouds in adjacent layers are maximally overlapped to form a continuous cloud and that groups of clouds separated by cloud-free layers are randomly overlapped [*Geleyn and Hollingsworth*, 1979]. The random overlap scheme assumes that all clouds are randomly overlapped regardless of whether there are clouds in vertically adjacent layers.

0148-0227/04/2003JD004040

[3] Cloud overlap has been studied using observations as well as models. For example, a statistical analysis of cloudiness observations for midlatitude clouds over oceans [*Tian and Curry*, 1989] favored the use of the maximum-random overlap scheme for vertically adjacent cloud layers. *Mace and Benson-Troth* [2002] examined cloud overlap using observations at two tropical sites, one midlatitude continental site and the North Slope of Alaska. At the tropical and midlatitude sites, they found that if the separation between cloud levels was small (<1 km) the maximum overlap assumption was favored, but that cloud fraction was best represented by something between the random overlap assumption and the maximum-random overlap assumption for larger separation distances. *Morcrette and Jakob* [2000] studied the effects of using RAN and MRAN on both radiation and the development of clouds in the ECMWF model and found large differences between the two treatments. *Stubenrauch et al.* [1997] implemented a version of MRAN in the GISS GCM and found that it provided slightly better agreement of the TOA radiative fluxes with satellite observations than the standard GISS treatment which uses a comparison of the predicted cloud fraction to a random number to determine whether a grid box is entirely cloudy or entirely cloud free [*Lacis and Oinas*,

1991]. *Weare* [2001] evaluated and compared changes in top-of-atmosphere net cloud radiative forcing resulting from changes of cloud water content and occurrences during the 1987 ENSO event between random overlap and a satellite- and surface-based monthly observed overlap. His analysis strongly suggested that accurate specification of overlap in a climate model is critical to the calculation of the appropriate radiative feedbacks due to changes of cloud water content and also cloud occurrence on different levels.

[4] While the effects of different forms of treating radiative fluxes through clouds have been studied in GCMs, there is no study to date of the effects of these treatments in photochemical models. A variety of schemes for treating clouds have been used in different photochemical models. For example, *Spivakovsky et al.* [2000] use International Satellite Cloud Climatology Project (ISCCP) cloud optical depths and distribute these uniformly between cloud top and 900 hPa. In order to determine the effects of the contributions of N cloud layers within a given column, they first perform N column calculations of photolysis frequencies (J-values) assuming only one layer of the column is filled with cloud and that it is thick enough to reflect all radiation. They then computed the average of the results weighted by these contributions. *Brasseur et al.* [1998] implemented a scheme which provides a parameterization for cloudy-sky photolysis frequencies at a pressure level that depends on the vertically averaged cloud cover and a total cloud extinction optical depth for clouds below, in and above that pressure level [*Chang et al.*, 1987] (also defined in *Brasseur et al.* [1998, equations (8), (9), and (10)]). The cloud extinction optical depth is calculated by *Brasseur et al.* [1998] as a function of the cloud fraction in each layer raised to the 3/2 power. This formulation for cloud optical depth has features that are similar to the random cloud overlap scheme developed by *Briegleb* [1992] and outlined below. *Berntsen and Isaksen* [1997] did not have cloud fraction from the GCM they used to drive the meteorology for their simulations, but generated a parameterization for cloud fraction from the optical depth given by the GCM. Then they averaged the J-values calculated for each cloud fraction. It is not clear from their paper, but it appears that this cloud fraction applies to an atmospheric column, rather than a grid box, so that their clouds are all vertically coherent, similar to the maximum overlap assumption. *Wild et al.* [2000] compared an implementation similar to that used in *Spivakovsky et al.* [2000] and *Chang et al.* [1987] with more exact calculations based on actual cloud optical depth and showed that the method used in *Spivakovsky et al.* [2000] overestimates photolysis frequencies above and below clouds by about 7–10% on a global average basis while the *Chang et al.* [1987] method gives reasonable results for a global average, but has errors in the midtroposphere. However, they only examined clouds that covered an entire horizontal grid box.

[5] The assumption that clouds cover an entire horizontal grid is the simplest assumption made in current chemical transport models (CTMs). In this approach (hereafter referred to as the linear assumption, LIN), the uniform cloud cover over the grid is assigned a cloud optical depth equal to the mean of the cloud free areas and cloudy areas in each layer [*Wild et al.*, 2000] which assumes that the actinic flux is linearly proportional to the cloud optical depth. This approach may introduce a large bias to the calculated photolysis frequencies compared to the weighted average photolysis frequencies under clear-sky and cloudy conditions with either maximum-random overlap or random overlap because of the nonlinear relationship between photolysis frequencies and cloud optical depth. Here, we use a photochemical model to examine the effect of assumptions regarding cloud overlap on photolysis frequencies and calculations of hydroxyl radical (OH).

[6] A detailed implementation of RAN requires an extensive set of computations. For example, if a column contains 3 layers with clouds, one would need to solve the radiative transfer equation in the clear sky fraction, in three columns with only one cloud layer each, in three columns with two overlapping cloud layers, and in one column with the three clouds superimposed vertically. In general, 2^n column radiative transfer calculations are necessary for a column with clouds in n layers. Several methods have been used to reduce the number of column calculations, however. For example, in the scheme of *Morcrette and Fouquart* [1986], the clear and cloudy reflectivities, R, and transmissivities, T, of a given layer are weighted according to the cloud fraction in the layer, i.e.,

$$R = (1 - C)R_{clr} + CR_{cdy} \tag{1}$$

$$T = (1 - C)T_{clr} + CT_{cdy} \tag{2}$$

where the subscripts *clr* and *cdy* refer to the clear and cloudy parts of the layer, respectively, and C is the cloud fraction for the layer. The downward-looking transmission of the clear-sky layer assuming direct radiation uses an effective zenith angle which depends on the amount of cloudiness and optical thickness in all layers above the layer [*Morcrette and Fouquart*, 1986]. The grid averaged reflectivities and transmissivities are then used in a single column radiation calculation. This scheme is followed in the shortwave radiation routine designed by *Fouquart and Bonnel* [1980]. *Morcrette and Fouquart* [1986] showed that the method provides a good approximation to the detailed random overlap method. A second method was used in the NCAR GCM [*Briegleb*, 1992]. In this method, the grid average optical depth τ_c' is approximated by

$$\tau_c' = \tau_c \times C^{3/2} \tag{3}$$

where τ_c is the cloud optical depth in the cloudy portion of the grid and C is the cloud fraction in each layer. This method, like the linear method employed in some CTM's requires only a single column radiative transfer calculation. *Briegleb* [1992] demonstrated that this method provides a reasonable approximation to a detailed random overlap calculation for the heating rate. Figure 1 shows a photolysis calculation using this approximate method for RAN and an exact calculation for RAN, for a number of cloud scenarios in a single column. For large cloud fractions, the scaling of cloud optical depth by cloud fraction to the 3/2 power is a good approximation for the exact calculation of RAN, but there are large errors for small cloud fraction. However, this method is one of the most widely used approximations for RAN in global CTMs [e.g., *Brasseur et al.*, 1998]. Therefore we employ it here for all global random overlap calculations (hereafter, RAN represents this approximate method, if not explicitly specified).

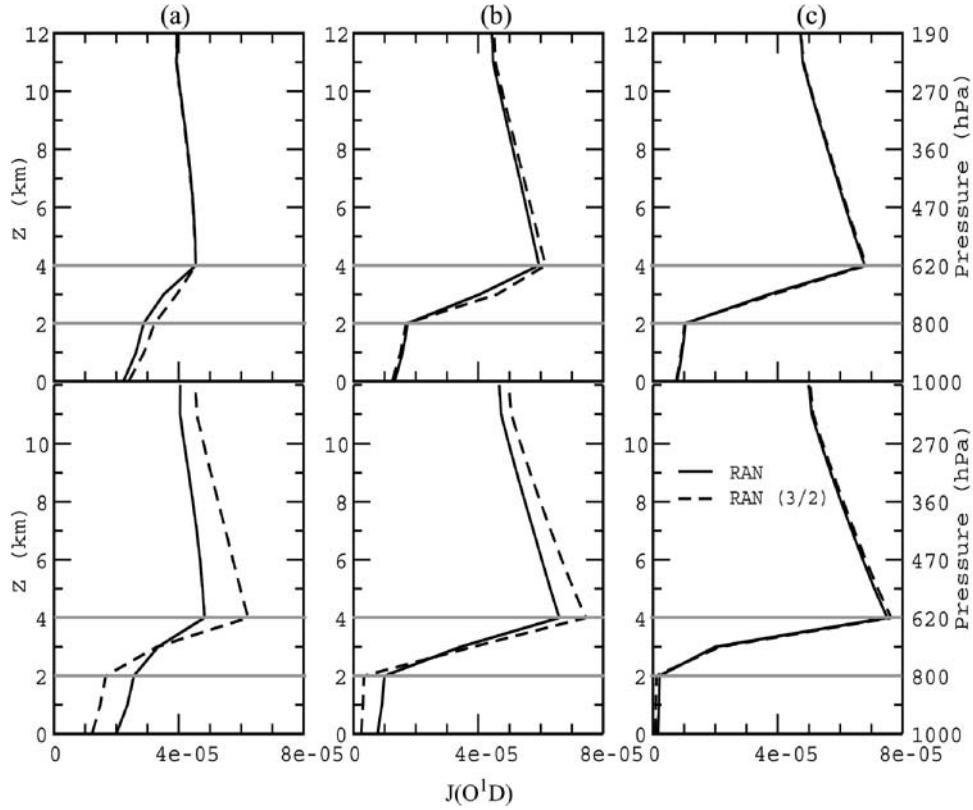

Figure 1. A comparison of the exact calculation of photolysis frequencies (in s^{-1}) with RAN (solid), and an approximation of RAN (dash), for the photolysis of O_3 to produce $O(^1D)$ at a zenith angle of 30°. Clouds are placed between 2–3 km and 3–4 km (cloud top and base are highlighted with gray lines). Column cloud fractions are (a) 0.1 and 0.2, (b) 0.5 and 0.5, and (c) 0.7 and 0.9, respectively. For the upper three panels, the cloud liquid water content is 0.2 gm^{-3}, and it is 1.2 gm^{-3} for the lower three panels.

[7] A detailed implementation of MRAN also requires a large set of column radiative transfer calculations. In MRAN, one converts a vertical profile of fractional cloudiness into a spectrum of column configurations with corresponding fractions (see illustration in Figure 2). Each layer for each configuration has either a full cloud fraction ($C = 1$) or is clear. A GCM column with n layers of vertically contiguous clouds, each with different cloud fractions, would require $n + 1$ column configurations, assuming that all clouds overlap to the maximum extent possible. Photolysis frequencies are then the weighted average of the $n + 1$ column radiation calculations. In practice, the number of cases treated is usually limited [*Collins*, 2001]. Here, we limit the number of cases treated to those with the largest 15 column area fractions. This simplification reduces the total computing time but does not introduce large errors because the fractional weights of those column configurations that are ignored are generally small. For example, in 1 year of meteorology data, over 90% of the atmospheric columns account for more than 90% of the calculated column area fractions. An alternative method for calculating MRAN might be to solve the equations using a bandmatrix method [*Zdunkowski et al.*, 1980, 1982].

2. One-Dimensional Test Cases

[8] The difference between photolysis frequencies calculated using different cloud overlap schemes is sensitive to cloud fraction as well as to solar zenith angle. These differences are illustrated for O_3 photolysis frequencies in Figures 3 and 4 for 0° solar zenith angle and 60° solar zenith angle, respectively. Results shown here were calculated using the 8-stream discrete ordinate model of *Madronich and Flocke* [1998]. Atmospheric conditions were based on the annual mean 45°N 1976 US standard atmosphere. Ozone, SO_2 and NO_2 column burdens were set to be 330 DU, 0.1 DU, and 0.1 DU, respectively. Surface albedo is 0.1 and no aerosols were included. Clouds were assumed to be full scattering only, with single scattering albedo = 0.9999 and asymmetry factor g = 0.85.

[9] In Figures 3a and 3b, clouds of liquid water path 360 gm^{-2} (mean optical depth = 54) are placed between 2–4 km with: (a) cloud fraction 0.1 for 2–3 km and 0.2 for 3–4 km; and (b) cloud fraction 0.8 for 2–3 km and 0.9 for 3–4 km. In Figure 3c cloud fraction is 0.2 for 2–3 km and 0.3 for 3–4 km, but the liquid water path is reduced to 40 gm^{-2} (mean optical depth = 6).

[10] Under clear-sky conditions, the vertical profile of the photolysis frequency for O_3 photolyzing to produce $O(^1D)$, $J(O^1D)$, has a weak maxima at about 5 km, as a result of the competition between the increase of the $O(^1D)$ quantum yield with temperature and the decrease in ultraviolet intensity towards the surface. When there is an optically thick cloud present, as in previous studies [e.g., *Liao et al.*, 1999], photolysis frequencies are enhanced above the cloud and reduced below the cloud.

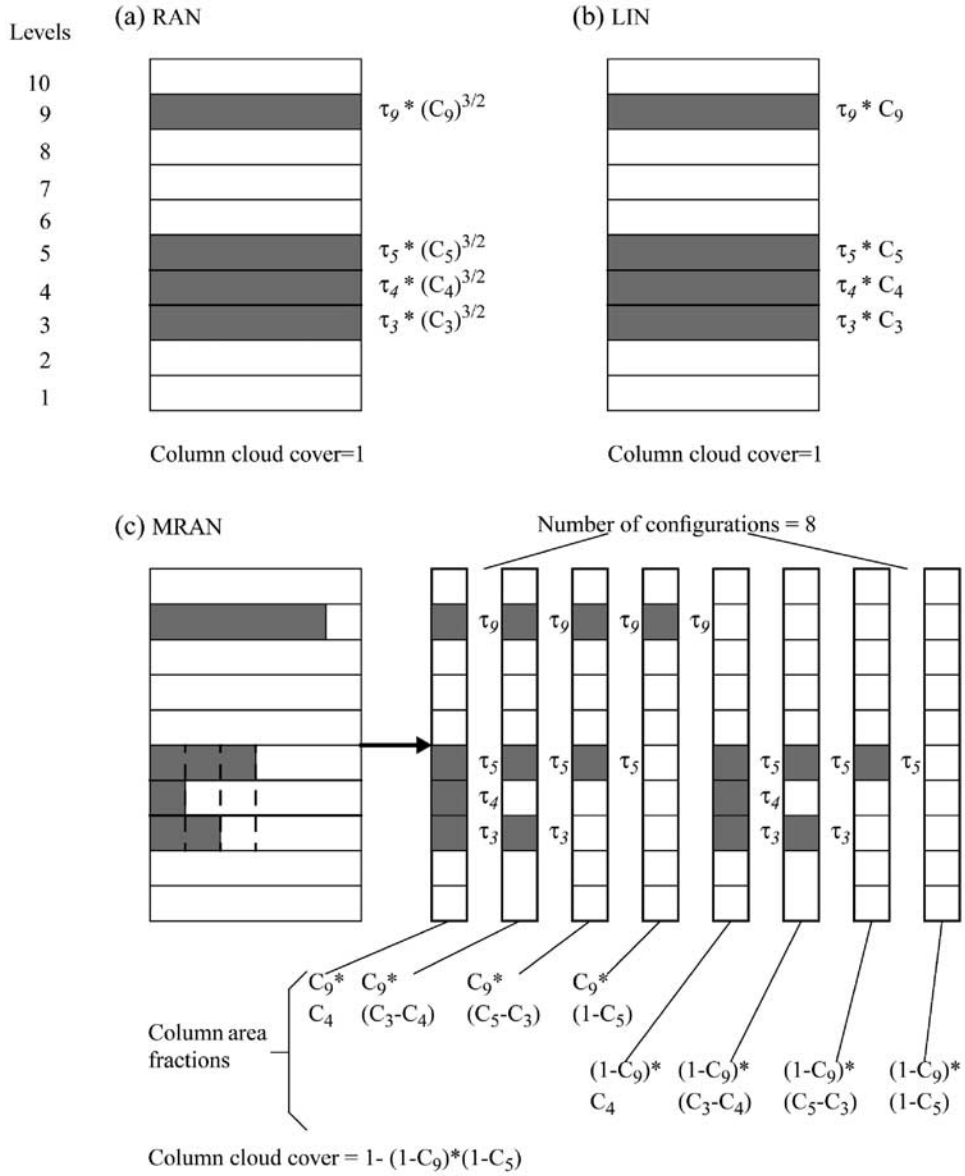

Figure 2. Illustration of implementation of cloud vertical treatments for actinic flux calculations: example of one column containing clouds at level 3, 4, 5 and 9. The cloud optical depth and fraction at each level are represented by τ_i and C_i, i = 1. . ., 9. For (a) an approximation of random overlap and (b) the linear assumption, uniform cloud cover is assumed and the corresponding cloud optical depth input for the radiation model is given on the right. Panel (c) illustrates the maximum-random overlap for this case which converts into 8 configurations. Fluxes are calculated for each configuration and then averaged, weighted by the corresponding column area fractions which are given below each column.

[11] For clouds with small cloud fraction as in Figure 3a, the reduction of $J(O^1D)$ below the cloud and the enhancement above the cloud are substantially smaller in MRAN than in RAN and LIN. The cloud albedo (reflectivity) is close to one in all three treatments for large cloud optical depths (>10). The effects of clouds in altering the intensity of solar radiation are overestimated in both RAN and LIN compared to MRAN, because clouds are spread uniformly over the layer in these two schemes so that the cloud cover (the fractional area of the column that is considered to be cloudy sky) is much larger than in MRAN. Photolysis frequencies in RAN are closer to those in MRAN than are those in LIN, because the scaling of cloud optical depth in RAN offsets some of the overestimation. The crossover altitude of photolysis frequencies for clear and cloudy skies occurs at descending altitudes from the cloud top for MRAN, LIN and RAN. On average, in the upper part of the troposphere, or above the cloud, there are more photons available for photochemistry in LIN and RAN than in MRAN, due to more reflection from the cloud below; but fewer photons below the cloud because less intensity is able to penetrate through the cloud in LIN and RAN.

[12] For clouds with large cloud fractions and with large cloud optical depth as in Figure 3b, the difference between the column cloud cover used in the three cloud treatments is small, so the calculated photolysis frequencies and the

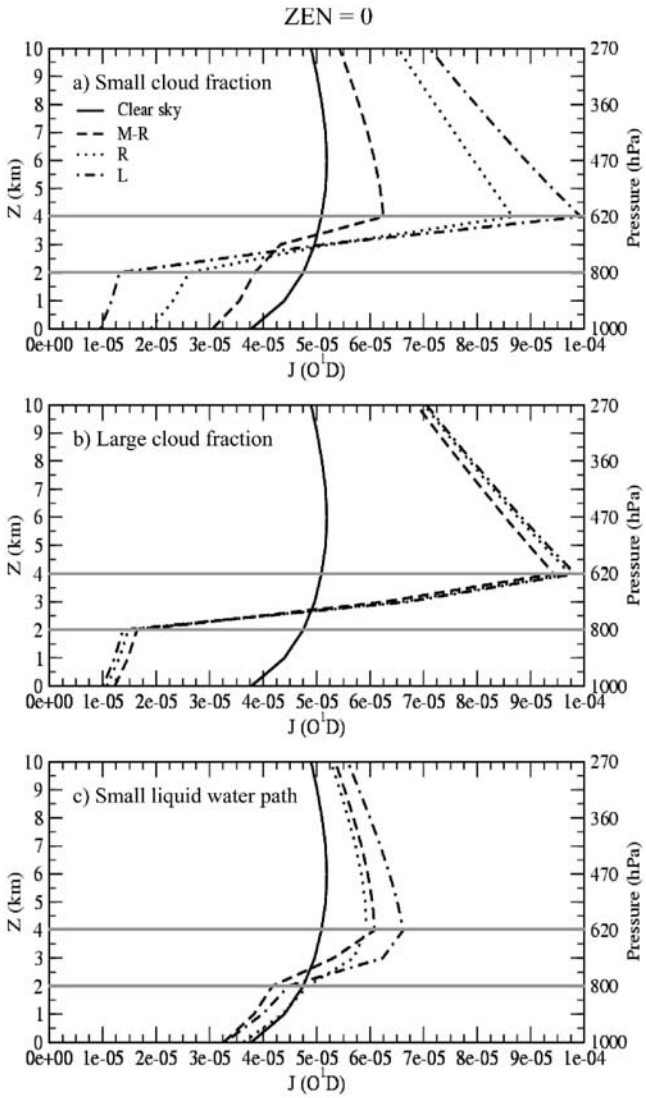

Figure 3. Photolysis frequency of ozone to form $O(^1D)$ (in s^{-1}) for clear sky and three types of overlap assumptions: M-R (maximum-random), R (random) and L (linear assumption) at a zenith angle equal to 0 degrees. Clouds are placed between 2–3 km and 3–4 km (cloud top and base are highlighted with gray lines), and the cloud fractions are (a) 0.2 and 0.3, and for (b) 0.8 and 0.9, respectively. Total liquid water path for (a) and (b) is 360 gm^{-2}. For (c) the cloud fractions are 0.2 and 0.3 with total liquid water path equal to 40 gm^{-2}.

altitudes at which the cloudy sky simulations crossover those for clear skies are very similar.

[13] In Figure 3c, the mean cloud optical depth is much smaller than that in Figures 3a and 3b. In MRAN, the cloud reflectivity increases significantly above that calculated for RAN and LIN, because the total cloud optical depth is larger when the clouds in adjacent layers are lined up. Even though the column cloud cover is smaller in MRAN, smaller photolysis frequencies are calculated with MRAN below the cloud and larger frequencies above the cloud than with RAN. However, larger column cloud cover in LIN still allows a larger above-cloud enhancement of $J(O^1D)$ than in MRAN.

[14] At the large zenith angles shown in Figure 4, the photolysis frequencies below the cloud are reduced more significantly in each of the cloud overlapping schemes due to a longer optical path, producing effects similar to those that occur with a thicker cloud optical depth. Compared to MRAN, the reduction in photolysis frequencies below cloud in RAN and LIN is enhanced, especially for small cloud fraction. Thus in Figures 4a and 4b, the difference in the photolysis frequencies between MRAN and LIN or RAN is more evident. In Figure 4c, MRAN gives the largest below-cloud photolysis frequencies, instead of the smallest frequencies as with overhead Sun. In general, the impact of clouds relative to clear sky photolysis frequencies is reduced for optically thick clouds in MRAN compared to RAN and LIN, but enhanced especially below cloud for optically thin clouds.

3. Global Effects of Cloud Overlap Treatment

[15] Changes in photolysis frequencies can impact tropospheric chemistry through a number of pathways. The most

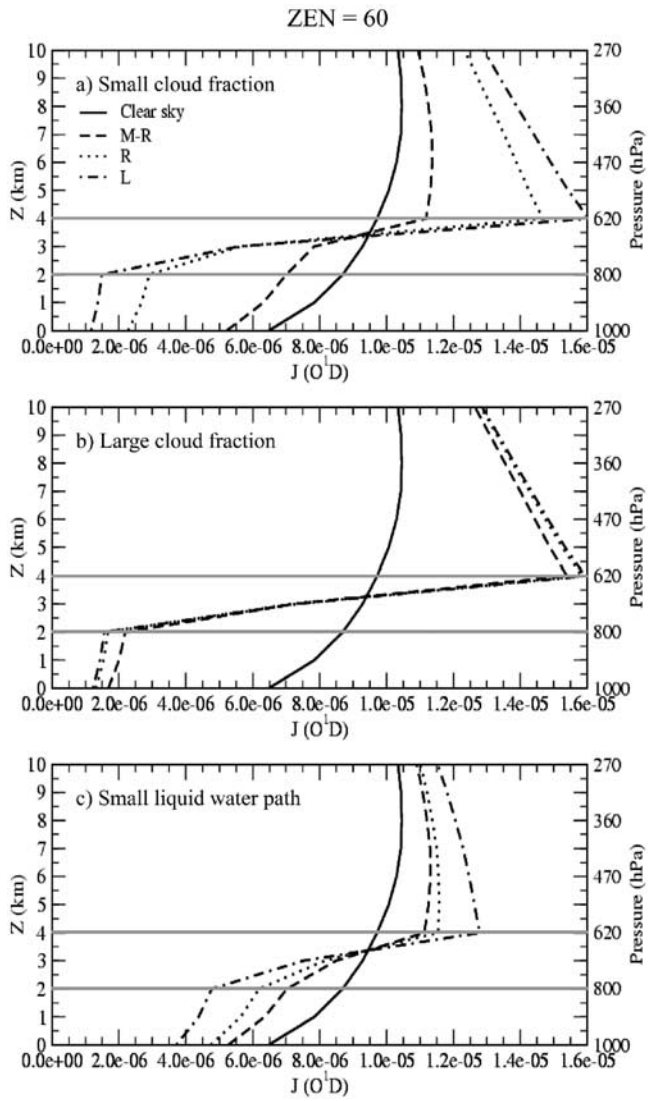

Figure 4. As for Figure 3, but with a zenith angle of 60 degrees.

Table 1. Aerosol Radiative Properties for Wavelengths from 300 to 400 nm

	Sulfate	OC	BC	Dust	Sea Salt
Single scattering albedo	0.97	1.0	0.53	0.65	0.95
Extinction efficiency	2.55	1.90	2.70	2.42	2.73
Effective radius (μm)	0.224	0.113	0.113	1.182	0.452

important photolysis frequencies are those that determine the concentrations of OH, since OH reacts with most pollutants to oxidize them to forms that eventually lead to their removal. These photolysis frequencies include the photolysis of O_3 to form $O(^1D)$ which reacts with H_2O to form OH and the photolysis of NO_2 to form an oxygen atom $O(^3P)$ which combines with O_2 to form O_3. One expects a significant perturbation to the concentration of OH if photolysis frequencies change as a result of the cloud overlap treatment through both these reactions and through intermediate products such as HCHO.

[16] To evaluate these effects we used the University of Michigan version of the Lawrence Livermore National Laboratory (LLNL) IMPACT model [*Liu and Penner*, 2002], modified to include a representation of tropospheric CO-CH_4-NO_x chemistry. This included the standard inorganic and methane reactions from *DeMore et al.* [1997]. The horizontal resolution of the model is 2° × 2.5°, and it has 46 layers vertically, including 23 layers in the stratosphere. Concentrations were specified for CO, CH_4, HCHO, H_2, O_3, H_2O_2 and NO_x. Steady state concentrations of NO, NO_2, N_2O_5, OH, HO_2 and CH_3O_2 were calculated diurnally based on the specified concentrations of the long-lived species. The numerical solution was obtained using methods described in *Sillman* [1991].

3.1. Fixed Species and Cloud Distributions

[17] The global distribution of tropospheric ozone was specified using the monthly averaged 3-D concentrations described in *Penner et al.* [1991] while monthly average stratospheric ozone (ozone > 100 ppb) was specified according to SBUV measurements [*McPeters*, 1993]. The tropospheric O_3 reflects the longitudinal gradients in the lower troposphere that are related to NO_x emissions. The latitudinal surface concentrations of CO were derived from the observations by the NOAA Climate Monitoring and Diagnostics Laboratory (CMDL) surface stations for 12 months. The vertical profile of CO was constructed on the basis of a variety of measurements made in the clean troposphere [*Logan et al.*, 1981]. This CO specification has reasonable latitudinal and seasonal variations. The concentration of CO near the surface is significantly higher than in the free troposphere, especially in the Northern Hemisphere (NH). We adopted the same specification for CH_4 as that used by *Spivakovsky et al.* [2000] by assuming uniform mixing ratios of 1645, 1655, 1715, and 1770 ppb from south to north with divisions at 32°S, the equator, and 32°N. Two different global average concentrations of NO_x were specified: 30 ppt and 100 ppt. We used typical low values for HCHO (100 ppt) and H_2O_2 (100 ppt) observed in the remote troposphere [*Weller et al.*, 2000; *Wang et al.*, 1998].

[18] Aerosol optical depth and single scattering albedo were calculated from monthly averaged aerosol column burdens from the ECHAM-GRANTOUR one-year simulation [*Penner et al.*, 2001, 2002] and specific aerosol radiative properties (see Table 1). The aerosol properties follow *Bian et al.* [2003] except for OC and BC, where we calculated the optical properties assuming Mie scattering for OC and BC and a log-normal size distribution with a geometric mean radius of 0.08 μm and a standard deviation of 1.45 [*Torres et al.*, 2002]. The refractive index was 1.8 + *i*0.3 for BC and 1.53 for OC. Relative humidity adjustments as described by *Penner et al.* [2002] for sulfate and sea salt aerosol are included. The global and annual mean aerosol optical depth is 0.374 and the single scattering albedo is about 0.9.

[19] Cloud liquid water content was calculated from a parameterization used in NCAR CCM [*Hack*, 1998]:

$$\rho_l = \rho_l^0 e^{(-z/h_l)} \tag{4}$$

where ρ_l^0 is equal to 0.18 gm^{-3}. The liquid water scale height, h_l is a time-independent, meridionally varying, empirically derived quantity, which is evaluated using:

$$h_l = A + B\cos^2\theta \tag{5}$$

where A = 1080 m, B = 2000 m, and θ is the latitude.

[20] We calculated relative humidity from the water vapor fields provided by the NASA Goddard Data Assimilation Office (DAO) data set for 1997–1998 (see *Liu and Penner* [2002] for a description of these fields) and then used this to parameterize the large scale stratiform cloud fraction according to *Sundqvist et al.* [1989]. In this parameterization, the large-scale stratiform cloud fraction is given by

$$C_{LS} = 1 - \sqrt{1 - \frac{RH - RH_c}{1 - RH_c}} \tag{6}$$

where RH is the relative humidity and RH_c is the threshold relative humidity for condensation specified as a function as pressure which was parameterized according to *Xu and Krueger* [1991]. For convective cloud fraction, a parameterization which uses the convective mass flux [*Xu and Krueger*, 1991] was adopted:

$$C_C = C_0 + C_1 \log_{10}(M_C) + C_2(\log_{10}(M_C))^2, \quad \text{if } M_C > 0.01 \text{ hPa h}^{-1}, \text{otherwise } C_C = 0 \tag{7}$$

where M_C is the convective mass flux (hPa h^{-1}), and the coefficients C_0, C_1, C_2 are given as a function of pressure. Total cloud fraction, C, in each grid cell was obtained from the combination of the large scale cloud fraction and convection cloud fraction by

$$C = 1 - (1 - C_{LS}) \times (1 - C_C) \tag{8}$$

where C_{LS} is the large scale cloud fraction and C_C is the convective cloud fraction. Annual mean liquid water path calculated from the model is compared with observations [*Weng and Grody*, 1994] in Figure 5. The geographic pattern is reproduced well by the parameterization. The observed maxima in liquid water path associated with tropical convection are captured as well as the NH

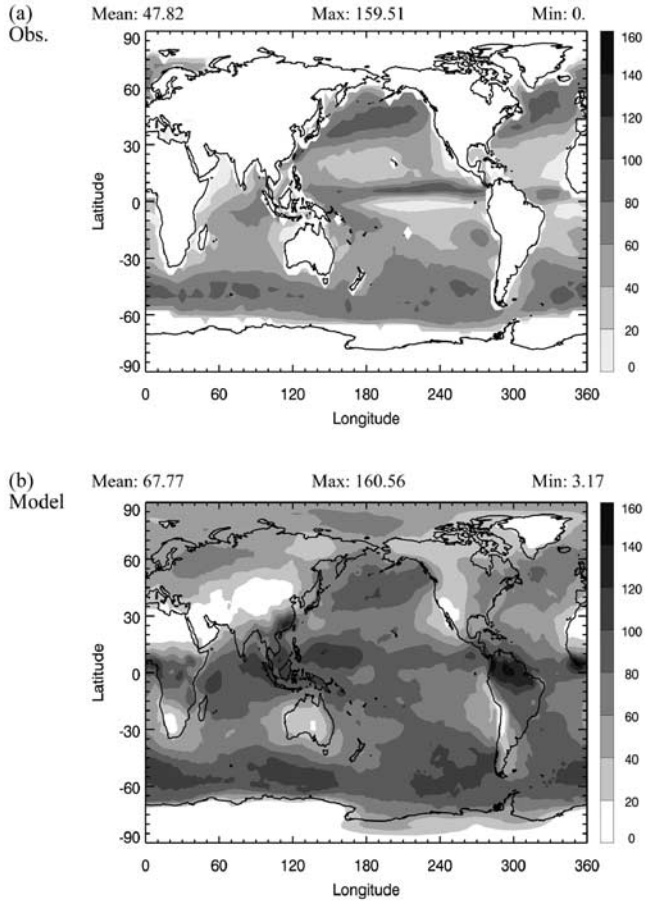

Figure 5. Geographic distribution of annual average liquid water path in gm^{-2}. (a) Observations over the ocean [*Weng and Grody*, 1994], and (b) model calculations over the whole domain.

extratropical cyclones and SH marine stratiform clouds near 50°S. The order of magnitude of the liquid water path is also in good agreement with the observations over the ocean. The annual and global mean liquid water path is about 68 gm^{-2}.

[21] The 2-dimensional cloud fraction calculated using MRAN and an exact implementation of RAN based on the 3-dimensional cloud fraction in equation (8) is shown in Figure 6 along with the International Satellite Cloud Climatology Project (ISCCP) observed cloud fraction. In order to compare with observations from the ISCCP, high-level clouds are ignored in the calculations at altitudes larger than 10 km between 30°S and 30°N, because high-level cloud amounts (with very low optical thickness <0.1 at 0.6 μm wavelength) are underestimated by a factor of 3 in the ISCCP data [*Liao et al.*, 1995]. The MRAN and RAN calculated cloud fractions generally reflect the geographical patterns of ISCCP observations. However, the MRAN calculated cloud fractions are normally lower than the ISCCP observations and the exact RAN calculated cloud fractions are higher than the ISCCP observations.

3.2. Photolysis Calculation

[22] The calculation of photolysis was parameterized in the global model. The method is essentially a linear or quasi-linear interpolation from a table of calculated photolysis frequencies for specified conditions. As in section 2, the calculated photolysis frequencies for the table were based on the Tropospheric Ultraviolet-Visible Model (TUV) [*Madronich and Flocke*, 1998]. The calculations used a pseudo-spherical discrete ordinates method [*Stamnes et al.*, 1988] with 8 streams. Total column O_3 and aerosol optical depth were allowed to vary in the calculations, but the vertical distribution remained constant.

[23] The parameterization provides photolysis frequencies for 56 tropospheric and stratospheric reactions as a function of the following parameters: θ, solar zenith angle; *z*, altitude; O_3, ozone column amount in Dobson units; *aero*, aerosol optical depth; *assa*, aerosol single scattering albedo; *alb*, surface albedo, assumed constant with wavelength; *CLa*, summed optical depth for all clouds above the

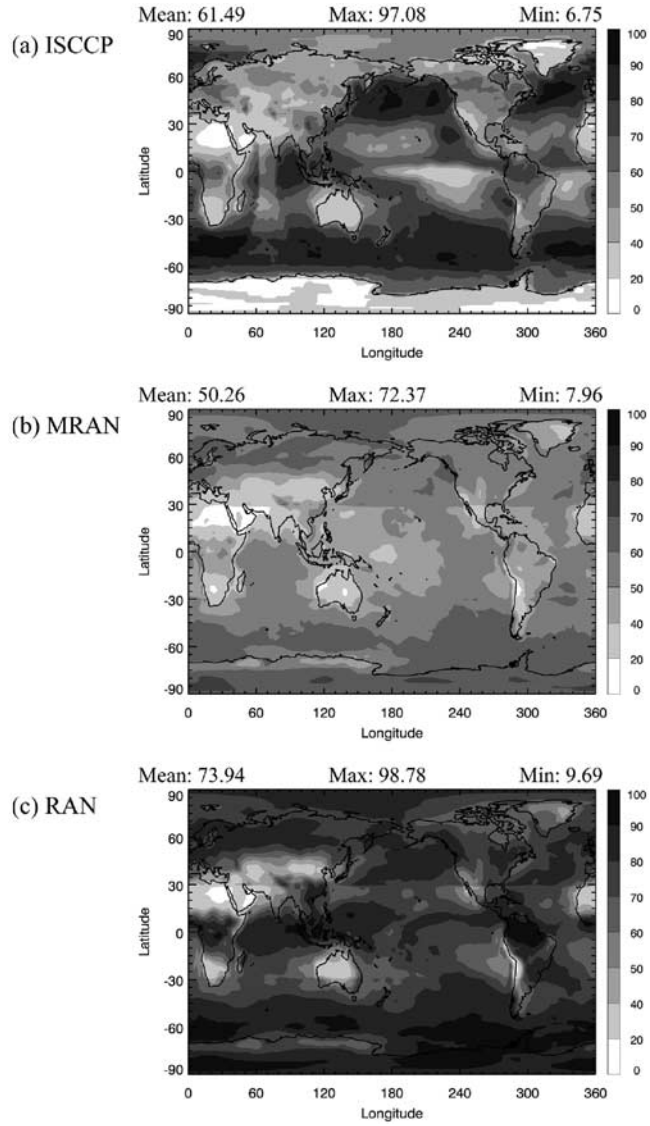

Figure 6. Annual average column cloud fraction (%). (a) Observations (International Satellite Cloud Climatology Project), (b) maximum-random overlap, and (c) an exact calculation for random overlap. The observation resolution is 2.5° × 2.5°, and the model resolution is 2° × 2.5°.

Table 2. Average Percentage Change in Clear-Sky Photolysis Frequencies Between the Look-Up Table Parameterization and the TUV Model Calculations

	$J(O^1D)$		$J(NO_2)$	
	Bias	s.d.	Bias	s.d.
Lower troposphere (>400 hPa)	0.4	1.8	0.1	1.6
Upper troposphere (100–300 hPa)	−0.1	1.2	0.3	0.6
Stratosphere (0.2–3 hPa)	0.2	2.7	0.3	3.5

specified altitude; *CLb*, summed optical depth for all clouds below the specified altitude; *CAa*, weighted average of the altitude of clouds above the specified altitude, weighted by vertical distribution of cloud optical depth, and expressed as the difference between the cloud altitude and the specified altitude; *CAb*, weighted average of the altitude of clouds below the specified altitude, weighted by the vertical distribution of cloud optical depth, and expressed as an altitude above ground; and *Y*, time of year.

[24] It is assumed that the impact of each individual parameter on photolysis frequencies can be represented as a multiplicative factor:

$$J(a_1, a_2, \ldots a_n) = f_1(a_1) f_2(a_2) \ldots f_n(a_n) = \prod_{i=1}^{n} f_i(a_i) \qquad (9)$$

[25] This format is consistent with the view that incoming solar radiation is calculated as a process of light attenuation through a series of extinction coefficients. Details of the parameterization are given in Appendix A.

[26] The photolysis look-up table was evaluated against the 8-stream TUV model. A series of column calculations were performed in which the solar zenith angle was varied between 0° and 94°, surface albedo was varied from 0. to 0.2, aerosol optical depth was varied from 0. to 0.76, aerosol single scattering albedo was varied from 0.75 to 0.99, and ozone column burden was varied from 250 to 410 DU. Table 2 shows the average bias between the table look-up method frequencies and the TUV model-calculated frequencies for clear-sky conditions for $J(O^1D)$ and $J(NO_2)$ below 400 hPa, from 100 to 300 hPa, and from 0.2 to 3 hPa. The average relative bias is less than 1% and the standard deviation of the bias is less than 2% in the troposphere. Under stratospheric conditions (0.2 to 3 hPa) the average relative bias is less than 0.5% and the standard deviation of the relative bias is less than 4%.

[27] The errors associated with treating the effects of clouds in the look-up table were examined by placing clouds at an altitude of 850 hPa (to characterize error associated with low clouds), at 600 hPa (to characterize errors associated with middle level clouds) and at 300 hPa (to characterize errors associated with high level clouds). To calculate the errors associated with clouds at these levels, we first compared the TUV model calculations to the look-up table photolysis frequencies assuming a zenith angle of 30° and cloud optical depths of 0, 0.5, 3, 10, and 32 for clouds at each representative level in a series of column tests. These cloud optical depths, which are nearly evenly distributed on a logarithmic scale of optical depth from 0 to 100, were tested because of the nonlinear relationship between photolysis frequencies and cloud optical depth. The average error over the altitude intervals associated with the lower (below 700 hPa), middle (400 hPa–700 hPa) and upper (above 400 hPa) troposphere for this set of clouds were calculated. If the clouds in the lowest two levels have an optical depth of less than 32 and high-level cloud has an optical depth of less than 10, then the errors are always less than ±6% for $J(O^1D)$. The look-up table tends to underestimate photolysis frequencies in the middle and upper troposphere and can both underestimate and overestimate photolysis frequencies in the lower troposphere. The individual column calculation errors are of less importance, however, if the conditions leading to a particular error occur only infrequently. They are also of less importance for the calculations of concern here, if they are approximately equal for the LIN, RAN, and MRAN calculations.

[28] The errors associated with the table look-up scheme in the global model were quantified in the following simplified manner. First, at each time step and for each column in the global model, cloud occurrence was characterized as either low (below 700 hPa), middle (400 hPa–700 hPa) or high (above 400 hPa) and the optical depth of the clouds in each of these layers was categorized as either zero, small (if it had an optical depth between 0 and 1), intermediate (optical depth 1 to 6), large (optical depth 6 to 18) or very large (optical depth greater than 18). Each category of cloud combination was then assigned the error associated with the above-described column tests for optical depths 0, 0.5, 3, 10, or 32 depending on whether the global model had zero, small, intermediate, large, or very large optical depths for each altitude range. Thus, for example, a column which has clouds below 700 hPa with an optical depth of 40, clouds between 400–700 hPa with an optical depth of 12, and clouds above 400 hPa with an optical depth of 2 would be assigned the error associated with the column calculation for clouds with optical depth 32, 10, and 3 placed at 850 hPa, 600 hPa, and 300 hPa in the column calculation. For an evaluation of the errors in the MRAN calculation, this error assignment was made for each possible column configuration.

[29] Global average errors were then estimated for a year of meteorology by summing the errors associated with each column, weighted by the surface area. Results for $J(O^1D)$ and $J(NO_2)$ are shown in Table 3. As this table shows, the errors in the look-up table photolysis frequencies are between −6% and +1%. However, the errors associated with MRAN, RAN and LIN are similar for each altitude range. Moreover, in this paper we are concerned with the error associated with the difference between LIN and MRAN and with the difference between RAN and MRAN. The error in the estimate of the difference between the calculation of RAN and MRAN or between LIN and MRAN can be estimated from standard statistical procedures for the propagation of errors. For example, the variance (or squared error) associated with the calculation of the percentage difference between RAN and MRAN, can be estimated from

$$\sigma^2_{RAN-MRAN} = \frac{\sigma^2_{RAN}}{J^2_{MRAN}} + \frac{J^2_{RAN}\sigma^2_{MRAN}}{J^4_{MRAN}} \qquad (10)$$

where σ^2_x is the variance associated with cloud overlap method x, and J_x is the J-value of interest in method x. The errors associated with the percentage differences estimated here cannot be estimated exactly without going

Table 3. Estimated Global Average Percentage Bias and Percentage Absolute Error Associated With the Cloudy-Sky Photolysis Look-Up Table Parameterization

	$J(O^1D)$			$J(NO_2)$		
	MRAN	RAN	LIN	MRAN	RAN	LIN
Lower troposphere (below 700 hPa)	1.4[a] (3.3)[b]	0.7(3.6)	1.4(4.2)	0.1(3.1)	−1.4(3.7)	−0.6(3.8)
Middle troposphere (700-400 hPa)	−1.8(2.3)	−2.7(2.8)	−2.8(2.9)	−3.6(4.1)	−5.4(5.5)	−5.6(5.8)
Upper troposphere (above 400 hPa)	−2.0(3.1)	−2.3(3.6)	−2.5(4.1)	−3.5(3.7)	−4.4(4.6)	−4.7(5.0)

[a]Numbers without parentheses indicate bias and are calculated as (J(look-up table) - J(TUV Model))/J(TUV Model) × 100.
[b]Numbers in parentheses indicate absolute error and are calculated as |J(look-up table) - J(TUV Model)|/J(TUV Model) × 100.

through an entire global calculation of J-values using the exact method, but by using the simplified method above (which was only carried out using a zenith angle of 30°), we can get some idea of how uncertain our estimates are. These are quoted as errors (though they are only approximate) in our estimates of the percentage difference in $J(O^1D)$ and $J(NO_2)$ below.

3.3. Results

3.3.1. $J(O^1D)$ and $J(NO_2)$

[30] The annual and zonal mean percentage changes of photolysis frequencies $J(O^1D)$ and $J(NO_2)$ between MRAN and RAN or LIN are shown in the Figures 7a and 7b. As noted in the introduction, observational studies have not been able to distinguish whether RAN or MRAN is preferred. However, for convenience, we reference our reported changes relative to the calculation using MRAN. For $J(O^1D)$, MRAN gives the largest J-values at the surface and the smallest J-values in the middle of the troposphere. When compared to MRAN, LIN underestimates photolysis frequencies more than does RAN at low altitudes. In the tropics, between 800 hPa to 500 hPa, RAN overestimates photolysis frequencies compared to MRAN and LIN underestimates them. This is because a larger mean optical depth is considered in LIN. The largest underestimation occurs for $J(O^1D)$ and is about 35 ± 9% in LIN and about 10 ± 3% in RAN at the surface. These differences are associated with regions of convection in the tropics, high occurrence of boundary-layer and cirrus clouds around 50°–60°N, and large-scale marine stratiform clouds at 50°S. Overestimation of J-values above clouds or in the upper portions of clouds occur at different altitudes as a function of latitude, due to a high occurrence of multiple cloud layers in midlatitudes but typically single deep clouds in the tropics.

[31] The impact of different cloud overlap schemes on $J(NO_2)$ is generally similar to that of $J(O^1D)$. However, the primary absorption by NO_2 takes place at longer wavelengths, near 380 nm, so that the photolysis of NO_2 has less dependence on Raleigh scattering and ozone absorption than does the photolysis of O_3 to produce $O(^1D)$. Also, the absorption cross section for $J(NO_2)$ is not strongly dependent on temperature as is that for $J(O^1D)$. The temperature effect reduces the above-cloud increment and below-cloud decrement by clouds on photolysis frequencies because temperature is decreasing with height. For a larger column cloud cover in RAN and LIN, the reduction of the impact of clouds by temperature is greater than for MRAN. So the thermal effect causes a smaller relative change of photolysis frequency between RAN or LIN and MRAN. In other words, there is less sensitivity of the photolysis frequency for O_3 to produce $O(^1D)$ to the cloud overlap assumption than for the photolysis frequency for NO_2.

[32] As a result, the impact of the cloud overlap treatment for $J(NO_2)$ is even more significant than it is for $J(O^1D)$. This is also true for other photolysis frequencies which have little temperature dependence, such as J(HCHO) etc. The largest overestimation for $J(NO_2)$ occurs around 400 hPa in the tropics and is about 25 ± 15% in RAN and about 35 ± 17% in LIN. There is also a small overestimation in the middle troposphere around 40°N–60°N.

[33] Figures 8a and 8b show the annual mean percentage change of $J(O^1D)$ and $J(NO_2)$ at the surface. LIN and RAN greatly underestimate photolysis frequencies in the tropics, by up to 60 ± 6% and 30 ± 7%, respectively, compared to MRAN, although in most tropical regions the difference in the calculation between RAN and MRAN is not larger than our simple estimate of the error associated with the table look-up. At mid latitudes (40°N–60°N) over NH continents, there is also a large underestimation which is mainly due to the presence of boundary-layer clouds with small cloud fraction during the summer in this region and is significantly larger than our estimate of the error associated with the look-up table (which is of order 5% for difference between both RAN and LIN and MRAN at these latitudes). The percentage change associated with large-scale stratiform clouds at 50°S and the sub-tropical cyclones over the northern Pacific is relatively small due to the large cloud fractions in these regions. RAN gives slightly larger photolysis frequencies at some surface areas than does MRAN while LIN generally produces smaller values. This is because RAN has a smaller cloud optical depth than LIN since, in our implementation of RAN, the cloud optical depth is multiplied by the cloud fraction to the 3/2 power and clouds in those regions are optically thin for RAN but are not necessarily optically thin for LIN. As shown in Figure 3c, for small optical depth, the increase of cloud reflectivity in MRAN may dominate the decrease of cloud fraction and give smaller photolysis frequencies at the surface than the other two schemes. The distribution of the effects of different cloud overlap schemes at the surface for $J(NO_2)$ is quite similar to the distribution for $J(O^1D)$, but the impact is enhanced, as discussed above.

3.3.2. OH Concentrations

[34] The 3D distribution of tropospheric OH was computed as a function of O_3, CO, NO_x ($NO + NO_2$), CH_4, HCHO, H_2O_2, H_2, water vapor, temperature, cloud cover and the density of the overhead ozone column at one-hour intervals. The solver calculates OH concentrations for each cloud configuration in MRAN and then computes the average concentration rather than computing the average

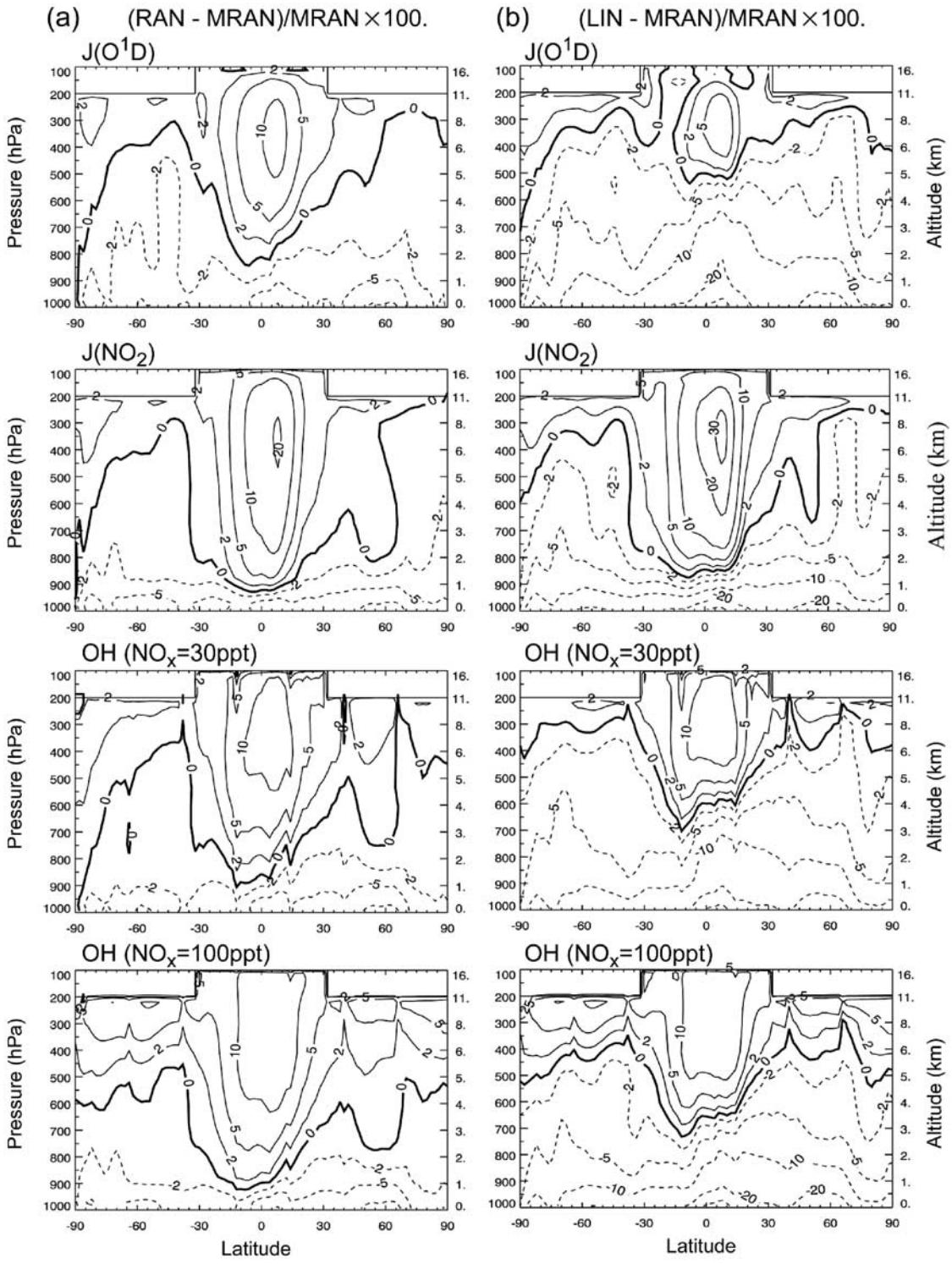

Figure 7. Annually and zonally averaged percentage changes (%) of photolysis frequencies $J(O^1D)$, $J(NO_2)$, and OH concentration at NO_x = 30 ppt and 100 ppt, between (a) random overlap and maximum-random overlap; (b) linear assumption and maximum-random overlap. Positive changes are represented by solid lines and negative changes by dashed lines. The photolysis model can be applied to the stratosphere, but calculations are only shown for the troposphere here. Contour intervals are −30, −20, −10, −5, −2, 0, 2, 5, 10, 20, 30.

photolysis frequencies and deriving OH from these. This implementation avoids the assumption of linearity between OH concentrations and photolysis frequencies, but requires more computing time.

[35] Annually and zonally averaged percentage changes of OH in RAN and LIN, compared to MRAN, are shown in Figures 7a and 7b for NO_x = 30 ppt and 100 ppt. Percentage changes at the surface are presented in Figures 8a and 8b.

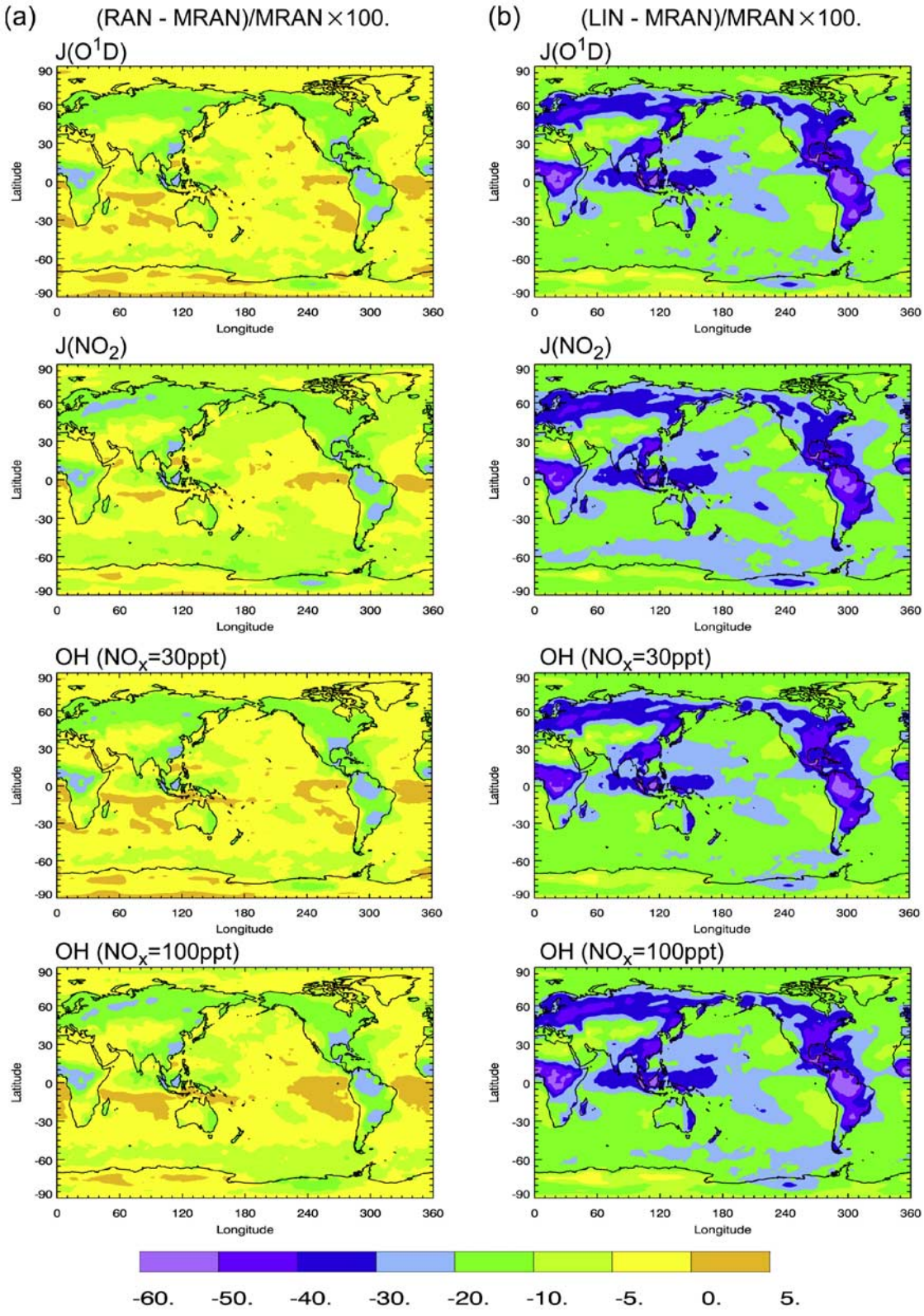

Figure 8. Annually averaged percentage changes (%) of photolysis frequencies $J(O^1D)$, $J(NO_2)$, and OH concentration at NO_x = 30 ppt and 100 ppt, at the surface between (a) random overlap and maximum-random overlap; (b) linear assumption and maximum-random overlap.

Table 4a. Percentage Change in the Volume-Weighted Tropospheric Mean OH Concentration From Different Cloud Overlap Schemes

	January (NO_x = 30ppt)		July (NO_x = 30ppt)		Annual (NO_x = 30ppt)		Annual (NO_x = 100ppt)	
100.*(XX[a] - MRAN)/MRAN	RAN	LIN	RAN	LIN	RAN	LIN	RAN	LIN
90S-32S	0.1	−2.0	−1.6	−3.2	0.1	−2.5	2.0	−0.1
32S-32N	6.2	5.3	3.3	−2.4	4.3	1.1	7.1	4.4
32N-90N	0.	−2.8	0.5	−4.8	0.3	−4.0	1.3	−2.3
Southern Hemisphere	3.2	1.6	1.4	−2.7	2.4	−0.1	4.9	2.8
Northern Hemisphere	3.6	2.5	2.8	−3.4	3.4	−0.8	5.5	2.0
Globe	3.2	1.8	2.3	−3.1	2.8	−0.4	5.1	2.4

[a]XX is RAN or LIN.

Tropospheric, hemispheric and semi-hemispheric means are given in Table 4a. Results represent the average integrated from the surface to 100 hPa between 32°S and 32°N and up to 200 hPa outside that region, weighted by the volume in each grid box. Table 4b gives the average changes in OH weighted by the CH_4 + OH reaction rate (mass of CH_4 times the reaction rate coefficient) in the troposphere [*Lawrence et al.*, 2001]. This weighting allows us to examine the importance of the calculated changes in OH for CH_4 removal rates, which depend more on the changes in OH near the surface and in the tropics. Volume weighted global means for specific levels are given in Table 5.

[36] Consistent with the changes of J-values, the enhancement of OH concentrations above clouds and the reduction below clouds in MRAN are less than those in RAN and LIN. LIN underestimates OH concentrations by up to 35% at the surface and overestimates OH concentrations by about 20% in the tropical middle troposphere. For RAN, the differences are less significant, about 15% and 20%, respectively. The distribution of OH concentration differences at the surface is quite similar to the distribution of photolysis frequency changes.

[37] For NO_x = 30 ppt, the tropospheric mean concentration of OH is 2.8% larger in RAN compared to MRAN, but 0.4% smaller in LIN (see Table 4a). The differences are small because positive differences between overlap assumptions in the midtroposphere completely or partly compensate for the negative differences in the lower troposphere. The tropospheric mean OH concentration weighted by the rate of the reaction of CH_4 with OH at each grid box, however, is underestimated by about 5.8% in LIN compared to MRAN (6.5% compared to RAN) but is approximately equal in RAN compared to MRAN (0.7%). Since the reaction of CH_4 with OH is the major destruction pathway of tropospheric CH_4, the lifetime of CH_4 would be prolonged in a CTM that uses the mean cloud optical depth in photolysis calculations. The differences between the OH concentrations in the Northern Hemisphere are somewhat larger than those in the Southern Hemisphere, reflecting the influence of the varying cloud cover in these two hemispheres on photolysis frequencies. The tropospheric mean change in the tropics (between 32°S and 32°N) is small, even though the largest overestimation and underestimation both arise in that region. Larger cloud liquid water paths result in larger differences in the mean OH concentration in July compared to January. Also the overestimation in LIN and RAN is predicted to occur at higher altitudes in July (see Table 5), due to the high occurrence of deep clouds that are associated with strong continental convection in the summer time. Similar to the comparison of photolysis frequencies, LIN gives the smallest annual mean OH concentration at the surface and overestimates OH, compared to MRAN, at a higher altitude than does RAN (Table 5).

[38] The NO_x mixing ratio does not directly affect the impact of cloud overlap on OH concentrations. However, a number of photolysis frequencies, e.g. $J(O^1D)$, $J(NO_2)$, J(HCHO), and $J(H_2O_2)$, all contribute to the dependence of OH on ultra-violet solar radiation, and the respective contribution by the various photolysis processes to the OH concentration varies with the NO_x mixing ratio (although $J(O^1D)$ plays a major role at all NO_x concentrations). In the present study, the dominant production of OH is from the photolysis of O_3 to form $O(^1D)$. The photodissociation of H_2O_2 is a minor source of OH. In addition, OH is recycled from HO_2 through the reaction with NO where HO_2 is produced from the photolysis of HCHO. This production path for OH is related to J(HCHO) and $J(NO_2)$. In the case with 30 ppt NO_x, the latter is a small term in the OH budget equation. Thus the effects of cloud overlap on OH concentration are mainly correlated to the changes of $J(O^1D)$. As NO_x increases to 100 ppt, the influence of J(HCHO) and

Table 4b. Percentage Change in Tropospheric Mean OH Concentration Weighted by the Reaction Rate for CH_4 + OH From Different Cloud Overlap Schemes

	January (NO_x = 30ppt)		July (NO_x = 30ppt)		Annual (NO_x = 30ppt)		Annual (NO_x = 100ppt)	
100.*(XX[a] - MRAN)/MRAN	RAN	LIN	RAN	LIN	RAN	LIN	RAN	LIN
90S-32S	−0.6	−3.8	−2.8	−6.1	−0.7	−4.7	−0.2	−3.6
32S-32N	4.8	0.8	0.2	−9.8	1.7	−5.5	3.2	−3.2
32N-90N	−2.0	−6.8	−1.6	−9.3	−1.6	−8.4	−1.1	−7.2
Southern Hemisphere	2.2	−1.5	0.1	−7.0	0.9	−4.3	2.0	−2.7
Northern Hemisphere	2.5	−1.2	−0.8	−10.7	0.4	−7.7	1.5	−5.6
Globe	2.2	−1.5	−0.4	−9.5	0.7	−5.8	1.8	−4.0

[a]XX is RAN or LIN.

Table 5. Percentage Change in Mean Volume-Weighted OH Concentration at Different Altitudes

	January (NO_x = 30ppt)		July (NO_x = 30ppt)		Annual (NO_x = 30ppt)		Annual (NO_x = 100ppt)	
100.×(XX[a] - MRAN)/MRAN	RAN	LIN	RAN	LIN	RAN	LIN	RAN	LIN
220 hPa	4.2	5.3	5.0	4.1	4.6	4.9	8.7	9.0
302 hPa	3.9	4.2	4.7	3.0	4.3	3.6	6.8	6.4
472 hPa	3.5	2.4	3.8	−1.0	3.8	1.0	4.8	2.7
675 hPa	2.8	−0.4	0.3	−7.7	1.7	−4.2	2.4	−2.5
813 hPa	1.0	−3.9	−1.7	−11.6	−0.5	−8.1	0.3	−6.7
875 hPa	0.0	−5.4	−2.6	−13.8	−1.6	−10.0	−0.9	−8.9
994 hPa	−2.0	−14.2	−7.8	−25.2	−5.2	−20.2	−5.4	−20.8

[a]XX is RAN or LIN.

$J(NO_2)$ increase as the recycling of HO_2 to OH has a larger impact on OH concentrations. The variations of OH concentrations between cloud overlap schemes are then sensitive to $J(O^1D)$, J(HCHO) and $J(NO_2)$. As a result, higher NO_x concentrations tend to enhance the impact of different cloud overlap schemes on OH concentrations (see Tables 4 and 5 and Figures 7 and 8), because of the different sensitivities of $J(O^1D)$, J(HCHO), and $J(NO_2)$ to the vertical placement of clouds, as explained in section 3.3.1. For the present study, we did not include the feedbacks between changes in OH on the distribution of NO_x. Nevertheless, the sensitivity study to NO_x concentrations demonstrates that there are relatively small differences in the change of OH between different cloud overlapping schemes for NO_x = 30 ppt and NO_x = 100 ppt. This implies that the exclusion of these feedbacks would not change our results significantly, in spite of the nonlinear relationship between NO_x and OH concentrations [e.g., *Kanakidou and Crutzen*, 1993].

4. Conclusions

[39] We have implemented three different cloud overlap schemes within a global chemical transport model to determine the effects of these schemes on photolysis frequencies and on calculated OH concentrations. Our results demonstrate that photolysis frequencies are increased in the upper tropical troposphere and decreased in the lower troposphere if clouds are assumed to be randomly overlapped or if a linear assumption is followed rather than the maximum-random overlap assumption. The increase in the upper tropical troposphere is relatively larger for a photolysis frequency without temperature dependence, such as the NO_2 photolysis frequency. The underestimate of photolysis frequencies near the surface is particularly large (of order 50 ± 10% and 50 ± 5% for $J(O^1D)$ and $J(NO_2)$, respectively, in the tropics and 50 ± 5% and 50 ± 3% for $J(O^1D)$ and $J(NO_2)$, respectively, over some continental midlatitude regions,) if the linear assumption is used. The random cloud overlap assumption leads to decreases of order 20 – 30% with similar standard deviations in these same regions.

[40] The underestimates and overestimates of photolysis frequencies at low and high altitudes, respectively, with the RAN and LIN schemes relative to the MRAN scheme are translated into underestimates and overestimates of OH concentrations in the troposphere. We find that the CH_4 + OH reaction rate-weighted OH concentration is increased by 0.9% and 2.0% in the Southern Hemisphere and increased by 0.4% and 1.5% in the Northern Hemisphere with the random overlap assumption assuming 30 ppt and 100 ppt NO_x, respectively. For the linear assumption, the reaction rate-weighted OH is reduced by 4.3% and 2.7% in the Southern Hemisphere and by 7.7% and 5.6% in the Northern Hemisphere for 30 ppt and 100 ppt NO_x, respectively.

[41] Compared to observations the random overlap assumption appears to overestimate cloud fractions while the maximum-random overlap assumption underestimates cloud fraction [*Mace and Benson-Troth*, 2002]. Thus, the small differences in the CH_4 + OH reaction rate-weighted OH concentration between the random overlap assumption and the maximum-random overlap assumption probably shows that the use of either of these two assumptions provides a reasonably accurate treatment of photolysis.

[42] However, the use of the nonphysically based linear assumption underestimates the CH_4 + OH reaction rate-weighted OH by as much as 5.8% on a global average basis. It is reasonable to assume that the net bias in global OH concentrations will cause errors of similar magnitude in the concentrations of long-lived species such as CH_4 and CO. These species are both removed from the atmosphere primarily by reactions with OH, so that an underestimate of the rate-weighted OH by 5.8% suggests an overestimate of the CH_4 tropospheric lifetime of similar magnitude and an overestimate of both CH_4 and CO concentrations. Similar errors will apply to other greenhouse gases that react with OH, with consequent implications for the climate system. It is less certain how the bias in model OH would affect the concentrations of shorter-lived organics or ozone. These species may be affected more by the changes in photolysis frequencies introduced by the use of different cloud overlap treatments in the lower troposphere, which are larger than tropospheric averages. Ozone is removed from the troposphere through reaction with OH, HO_2 and photolysis to produce $O(^1D)$ (followed by reaction with H_2O), all of which are affected by model representation of clouds. Photochemical production of ozone may also be affected by OH and by photolysis frequencies. However, any inferred bias in model ozone would be speculative at this point and dependent on the precursors.

[43] Our present study demonstrates the importance of cloud overlap in photochemical models by comparing three commonly used overlap schemes. Observations have not conclusively demonstrated whether the random overlap or the maximum-random overlap treatment is more realistic.

Bergman and Rasch [2002] propose a scheme based on a combination of the random and maximum-random overlap schemes. However, this scheme must prescribe parameters to which the calculated radiative fluxes are strongly sensitive. Therefore, further research on both observations and parameterizations of cloud overlap are needed, so that the uncertainties in global models can be reduced in the future.

Appendix A

[44] Interpolation of the photolysis frequencies from tabulated values is based on a standard 1st-order Taylor expansion:

$$J(a_i) = J\left(a_1^o, a_2^o, \ldots a_n^o\right) + \sum_{i=1}^{n} \frac{\partial J\left(a_1^o, a_2^o, \ldots a_n^o\right)}{\partial a_i}\left(a_i - a_i^o\right) \quad \text{(A1)}$$

where a_i represents the parameter values to be evaluated and a_i^0 represents tabulated values of the parameter. This first-order expansion (requiring a bilinear interpolation) leads to problems if the partial derivatives dJ/da_i are regarded as constant parameters. The 1st-order expansion results in a sum of adjustment factors for individual parameters, and blows up when the individual adjustments are large. (For example, a very large cloud optical depth combined with a large ozone column amount can lead to a photolysis rate less than zero). These errors occur when the 2nd-order and higher cross-partial derivatives between two parameters cannot be ignored.

[45] An improved interpolation that accounts for the higher-order mixed partial derivatives can be derived by taking advantage of the functional form shown in equation (9). The first partial derivatives can be expressed as

$$\frac{\partial J}{\partial a_i} = \frac{f_i'}{f_i} J \quad \text{(A2)}$$

where f_i' represents the derivative of the function f_i (a_i) in equation (9). Photolysis frequencies for the specified parameters a_i can be derived from the following modified Taylor expansion:

$$\begin{aligned} J\left(a_1, a_2^0, \ldots a_n^o\right) &= J\left(a_1^o, a_2^0, \ldots a_n^o\right) + \frac{\partial JJ\left(a_1^o, a_2^0, \ldots a_n^o\right)}{\partial a_1}\left(a_1 - a_1^0\right) \\ &= J\left(a_1^o, a_2^0, \ldots a_n^o\right)\left(1 + \frac{f_1'}{f_1}\left(a_1 - a_1^0\right)\right) \end{aligned} \quad \text{(A3a)}$$

$$\begin{aligned} J\left(a_1, a_2, \ldots a_n^o\right) &= J\left(a_1, a_2^o, \ldots a_n^o\right) + \frac{\partial J\left(a_1, a_2^o, \ldots a_n^o\right)}{\partial a_2}\left(a_2 - a_2^0\right) \\ &= J\left(a_1^o, a_2^o, \ldots a_n^o\right)\left(1 + \frac{f_1'}{f_1}\left(a_1 - a_1^0\right)\right) \\ &\quad \cdot \left(1 + \frac{f_2'}{f_1}\left(a_2 - a_2^0\right)\right) \end{aligned} \quad \text{(A3b)}$$

and so on, arriving at the solution

$$J(a_1, a_2, \ldots a_n) = J\left(a_1^o, a_2^o, \ldots a_n^o\right) \prod_{i=1}^{n}\left(1 + \frac{f_i'}{f_i}\left(a_i - a_i^0\right)\right) \quad \text{(A4a)}$$

(A similar, though less complete expansion can be developed by extending the original Taylor expansion in equation (A1) to include the 2nd-order cross terms, and evaluating with equation (9).)

[46] A slightly modified form of equation (A4a) is used to calculate photolysis frequencies by interpolating from tabulated values. The modified form is:

$$\begin{aligned} J(a_1, a_2, a_3, a_4, \ldots a_n) &= J\left(a_1, a_2, a_3^o, a_4^o \ldots a_n^o\right) \\ &\quad \cdot \prod_{i=3}^{n} p_i\left(a_1, a_2, a_3^o \ldots a_i, \ldots a_n^o\right) \end{aligned} \quad \text{(A4b)}$$

$$\begin{aligned} p_i\left(a_1, a_2, a_3^o \ldots a_i, \ldots a_n^o\right) &= 1 + \frac{f_i'}{f_i}\left(a_i - a_i^0\right) \\ &= \frac{J\left(a_1, a_2, a_3^o \ldots a_i, \ldots a_n^o\right)}{J\left(a_1, a_2, a_3^o \ldots a_i^o, \ldots a_n^o\right)} \end{aligned} \quad \text{(A4c)}$$

Equations (A4b) and (A4c) are used to derive photolysis frequencies (J) by interpolation from tabulated values. The parameters a_1 and a_2 represent solar zenith angle and altitude, while a_i for i equal to three or higher represent other input parameters. The values for $J(a_1, a_2, a_3^0, a_4^0, \ldots a_i^0, \ldots a_n^0)$ and $J(a_1, a_2, a_3^0, a_4^0, \ldots a_i, \ldots a_n^0)$ are found by bilinear and trilinear interpolation from tabulated photolysis frequencies. As described above, the tabulation includes values for an array of zenith angles (a_1), altitudes (a_2) and each individual input parameter (a_i), while all other parameters are at reference values $(a_3^0, \ldots, a_n^0)$.

[47] **Acknowledgments.** We wish to thank the two anonymous reviewers for their careful reading of the manuscript and for their thoughtful and helpful comments. This work was supported by the DOE ACP Program and the DOE ARM Program.

References

Bergman, J. W., and P. J. Rasch (2002), Parameterizing vertically coherent cloud distributions, *J. Atmos. Sci.*, *59*, 2165–2182.

Berntsen, T. K., and I. S. A. Isaksen (1997), A global three-dimensional chemical transport model for the troposphere: 1. Model description and CO and ozone results, *J. Geophys. Res.*, *102*, 21,239–21,280.

Bian, H., M. J. Prather, and T. Takemura (2003), Tropospheric aerosol impacts on trace gas budgets through photolysis, *J. Geophys. Res.*, *108*(D8), 4242, doi:10.1029/2002JD002743.

Brasseur, G. P., D. A. Hauglustaine, S. Walters, P. J. Rasch, J.-F. Muller, C. Granier, and X. X. Tie (1998), MOZART, a global chemical tracer model for ozone and related chemical tracers: 1. Model description, *J. Geophys. Res.*, *103*, 28,265–28,289.

Briegleb, B. P. (1992), Delta-Eddington approximation for solar radiation in the NCAR community climate model, *J. Geophys. Res.*, *97*, 7603–7612.

Chang, J. S., R. A. Brost, I. S. A. Isaksen, S. Madronich, P. Middleton, W. R. Stockwell, and C. J. Walcek (1987), A three-dimensional Eulerian acid deposition model: Physical concepts and formulation, *J. Geophys. Res.*, *92*, 14,681–14,700.

Collins, W. D. (2001), Parameterization of generalized cloud overlap for radiative calculations in general circulation models, *J. Atmos. Sci.*, *58*, 3224–3242.

DeMore, W. B., S. P. Sander, D. M. Golden, R. F. Hampson, M. J. Kurylo, C. J. Howard, A. R. Ravishankara, C. E. Kolb, and M. J. Molina (1997), Chemical kinetics and photochemical data for use in stratospheric modeling, *JPL*, *97-4*.

Fouquart, Y., and B. Bonnel (1980), Computation of solar heating of the Earth's atmosphere: A new parameterization, *Contrib. Atmos. Phys.*, *53*, 35–62.

Geleyn, J. F., and A. Hollingsworth (1979), An economical analytical method for the computation of the interaction between scattering and line absorption of radiation, *Contrib. Atmos. Phys.*, *52*, 1–16.

Hack, J. J. (1998), Sensitivity of the simulated climate to a diagnostic formulation for cloud liquid water, *J. Clim.*, *11*, 1497–1515.

Jakob, C., and S. A. Klein (1999), The role of vertically varying cloud fraction in the parameterization of microphysical processes in the ECMWF model, *Q. J. R. Meteorol. Soc.*, *125*(555), 941–965.

Kanakidou, M., and P. J. Crutzen (1993), Scale problems in global tropospheric chemistry modeling: Comparison of results obtained with a three-dimensional model, adopting longitudinally uniform and varying emissions of NO_x and NMHC, *Chemosphere*, *26*, 787–801.

Lacis, A. A., and V. Oinas (1991), A description of the correlated k distribution method for modeling nongray gaseous absorption, thermal emission, and multiple scattering in vertically inhomogeneous atmospheres, *J. Geophys. Res.*, *96*, 9027–9063.

Lawrence, M. G., P. J. Jöckel, and R. Von Kuhlmann (2001), What does the global mean OH concentration tell us?, *Atmos. Chem. Phys.*, *1*, 37–49.

Liao, H., Y. L. Yung, and J. H. Seinfeld (1999), Effects of aerosols on tropospheric photolysis rates in clear and cloudy atmospheres, *J. Geophys. Res.*, *104*, 23,697–23,707.

Liao, X., W. B. Rossow, and D. Rind (1995), Comparison between SAGE II and ISCCP high-level clouds: 1. Global and zonal mean cloud amounts, *J. Geophys. Res.*, *100*, 1121–1135.

Liu, X., and J. E. Penner (2002), Effect of Mount Pinatubo H_2SO_4/H_2O aerosol on ice nucleation in the upper troposphere using a global chemistry and transport model, *J. Geophys. Res.*, *107*(D12), 4141, doi:10.1029/2001JD000455.

Logan, J. A., M. J. Prather, S. C. Wofsy, and M. B. McElroy (1981), Tropospheric chemistry: A global perspective, *J. Geophys. Res.*, *86*, 7210–7254.

Mace, G. G., and S. Benson-Troth (2002), Cloud-layer overlap characteristics derived from long-term cloud radar data, *J. Clim.*, *15*, 2505–2515.

Madronich, S., and S. Flocke (1998), The role of solar radiation in atmospheric chemistry, in *Handbook of Environmental Chemistry*, edited by P. Boule, pp. 1–26, Springer-Verlag, New York.

McPeters, R. (1993), Ozone profile comparisons, in *The Atmospheric Effects of Stratospheric Aircraft: Report of the 1992 Models and Measurements Workshop*, edited by M. J. Prather and E. E. Remsberg, *NASA Ref. Publ.*, *1292*, D1–D37.

Morcrette, J.-J., and Y. Fouquart (1986), The overlapping of cloud layers in shortwave radiation parameterizations, *J. Atmos. Sci.*, *43*(4), 321–328.

Morcrette, J.-J., and C. Jakob (2000), The response of the ECMWF model to changes in the cloud overlap assumption, *Mon. Weather Rev.*, *128*, 1707–1732.

Penner, J. E., C. S. Atherton, J. Dignon, S. J. Ghan, J. J. Walton, and S. Hameed (1991), Tropospheric nitrogen—A three-dimensional study of sources, distributions, and deposition, *J. Geophys. Res.*, *96*, 959–990.

Penner, J. E., et al. (2001), Aerosols, their direct and indirect effects, in *Climate Change 2001: The Scientific Basis*, edited by H. T. Houghton et al., pp. 289–416, Cambridge Univ. Press, New York.

Penner, J. E., et al. (2002), A comparison of model- and satellite-derived aerosol optical depth and reflectivity, *J. Atmos. Sci.*, *59*, 441–460.

Rotstayn, L. D. (1997), A physically based scheme for the treatment of stratiform clouds and precipitation in large-scale models: 1. Description and evaluation of the microphysical processes, *Q. J. R. Meteorol. Soc.*, *123*(541), 1227–1282.

Sillman, S. (1991), A numerical solution to the equations of tropospheric chemistry based on an analysis of sources and sinks of odd hydrogen, *J. Geophys. Res.*, *96*, 20,735–20,744.

Spivakovsky, C. M., et al. (2000), Three-dimensional climatological distribution of tropospheric OH: Update and evaluation, *J. Geophys. Res.*, *105*, 8931–8980.

Stamnes, K., S. Tsay, W. J. Wiscombe, and K. Jayaweera (1988), Numerically stable algorithm for discrete-ordinate method radiative transfer in multiple scattering and emitting layered media, *Appl. Opt.*, *27*, 2502–2509.

Stubenrauch, C. J., and W. B. Rossow (1997), Implementation of subgrid cloud vertical structure inside a GCM and its effect on the radiation budget, *J. Clim.*, *10*, 273–287.

Sundqvist, H., E. Berge, and J. E. Kristiansson (1989), Condensation and cloud parameterization studies with a mesoscale numerical weather prediction model, *Mon. Weather Rev.*, *117*, 1641–1657.

Tian, L., and J. Curry (1989), Cloud overlap statistics, *J. Geophys. Res.*, *94*, 9925–9936.

Torres, O., P. K. Bhartia, J. R. Herman, A. Sinyuk, P. Ginoux, and B. Holben (2002), A long-term record of aerosol optical depth from TOMS observations and comparison, *J. Atmos. Sci.*, *59*, 398–413.

Wang, J. H., and W. B. Rossow (1998), Effects of cloud vertical structure on atmospheric circulation in the GISS GCM, *J. Clim.*, *11*(11), 3010–3029.

Wang, Y., J. A. Logan, and D. J. Jacob (1998), Global simulation of tropospheric O_3-NO_x-hydrocarbon chemistry: 2. Model evaluation and global ozone budget, *J. Geophys. Res.*, *103*, 10,727–10,755.

Weare, B. C. (2001), Effects of cloud overlap on radiative feedbacks, *Clim. Dyn.*, *17*, 143–150.

Weller, R., O. Schrems, A. Boddenberg, S. Gäb, and M. Gautrois (2000), Meridional distribution of hydroperoxide and formaldehyde in the marine boundary layer of the Atlantic (48°N–35°S) measured during the Albatross campaign, *J. Geophys. Res.*, *105*, 14,401–14,412.

Weng, F., and N. C. Grody (1994), Retrieval of cloud liquid water using the special sensor microwave imager (SSM/I), *J. Geophys. Res.*, *99*, 25,535–25,551.

Wild, O., X. Zhu, and M. J. Prather (2000), Fast-J: Accurate simulation of in- and below-cloud photolysis in tropospheric chemical models, *J. Atmos. Chem.*, *37*, 245–282.

Xu, K. M., and S. K. Krueger (1991), Evaluation of cloudiness parameterizations using a cumulus ensemble model, *Mon. Weather Rev.*, *119*(2), 342–367.

Zdunkowski, W. G., R. M. Welch, and G. Korb (1980), An investigation of the structure of typical two-stream-methods for the calculation of solar fluxes and heating rates in clouds, *Contrib. Atmos. Phys.*, *53*, 147–166.

Zdunkowski, W. G., W.-G. Panhans, R. M. Welch, and G. Korb (1982), A radiation scheme for circulation and climate models, *Contrib. Atmos. Phys.*, *55*, 215–238.

Y. Feng, X. Liu, J. E. Penner, and S. Sillman, Department of Atmospheric, Oceanic, and Space Sciences, University of Michigan, Ann Arbor, MI 48109-1349, USA. (penner@umich.edu)